Characterization of MEMS piston mirror arrays with comb drive actuator

S. Francés González*, M. Nitzsche, A. Bajpai, A. S. Pranti, A. Neudert, P. Duerr
Fraunhofer IPMS, Maria-Reiche-Str. 2, D-01109 Dresden, Germany

ABSTRACT

Nowadays virtual, augmented and mixed reality applications are becoming more and more widespread.With this, the requirements for image quality are getting more demanding, leaving room for improvement of the user experience of the existing systems. While many research groups and companies try to improve on fixed-focus stereo image systems, we propose to make use of real holography as the best possible solution providing all depth cues automatically in a consistent way. Within such holographic display systems, a spatial light modulator (SLM) is re-shaping the incident light generating the desired images. As SLMs with the required properties are not commercially available today, a novel device is being developed within the Horizon 2020 'REALHOLO' project funded by the European Union: a MEMS micromirror Array (MMA) with 8 million phase-shifting pixels based on a novel comb drive micro actuator concept. Earlier theoretical work and simulations had showed clear perspectives for a superior performance in comparison to other SLM technologies allowing high frame rates and high precision wave front modulation. By now the first samples of proof-of-concept MMA chips have been fabricated and in this paper we present experimental characterization results: microscope and SEM images, quasi-static response curves measured by white light interferometry (WLI) as well as the dynamic properties like resonance frequency and damping measured by laser doppler vibrometry (LDV). In addition an addressing approach for a minimum mirror settling time is also investigated. We discuss the impact of fabrication tolerances on the overall precision together with the response curve dependency on design parameters and compare the experimental results to simulations.

Keywords: MEMS, micromirror array, piston mode, phase modulation, comb drive actuator, spatial light modulator, computer generated holography

1. INTRODUCTION

Holography, invented in 1947 by Dennis Gabor, is a technique that uses interference and diffraction to record and reconstruct the full light wavefronts [1]. At that time holography was purely analog but in the late of 1980s the emerging SLM technologies, Charged-Coupled Device (CCD) image sensors and increasingly powerful computers make possible to digitally capture, process and display holograms [2]. In Computer-Generated Holography (CGH) a fringe pattern is calculated and transferred to a spatial light modulator (SLM). The SLM diffracts the light wave to yield an optical wavefront [3] that in the far field evolves into the desired image. Many applications make already profit of digital holography for example in the areas of microscopy [4] or interferometry [5]. In addition, the interest on displaying three-dimensional (3D) information for virtual, augmented and mixed reality applications, providing different visual information depending on the viewer's eye position and gaze, has been growing over the last years. 3D displays comprise stereoscopic displays, volumetric and holographic displays. Stereoscopic and volumetric displays are already commercially available but they suffer from several drawbacks: eye strain and fatigue due to the accommodation-convergence conflict are present in stereo displays and the dimension limitation is a disadvantages in the volumetric displays. On the other hand, holographic displays taking the advantages of CGHs provide all depth cues that a real 3D scene involves, altough they are still on the level of prototypes [6].

The ideal SLM would be a modulator allowing a multi-level precise phase control of the incoming coherent light at a high frame rate and precision. To limit efforts linked to the huge amount of data required to generate a CGH to manageable levels, the solution proposed here is to provide only a small 'viewing window' for the user's eyes with image content (see Figure 1 and [7]).

*sara.frances-gonzalez@ipms.fraunhofer.de; phone +49 351 8823-472; https://www.ipms.fraunhofer.de

This is the author's version of this paper. Please find the original here:

Proceedings Volume 12899, MOEMS and Miniaturized Systems XXIII; 128990D (2024)
https://doi.org/10.1117/12.3000871
Event: SPIE OPTO, 2024, San Francisco, California, United States

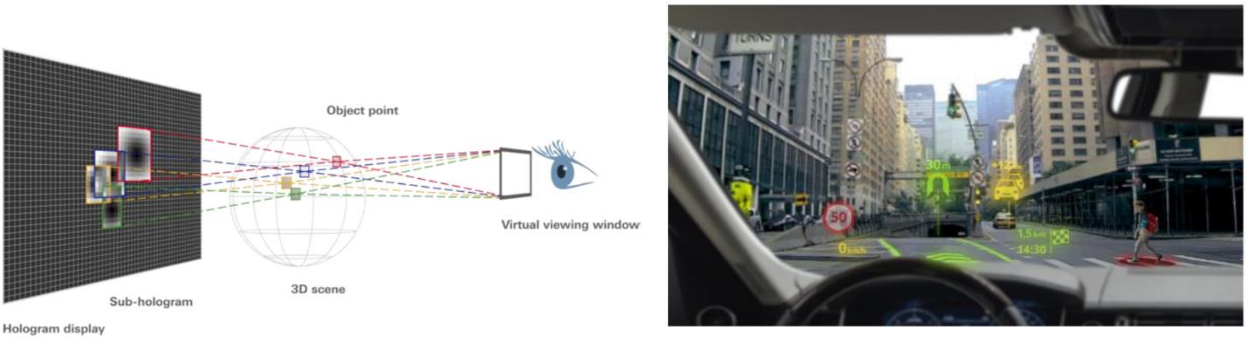

Figure 1: holographic display concept based on virtual viewing-window [8] and automotive mixed reality head-up display (HUD, artist's impression)

Although there are commercial SLMs already available on the market, none of them fully meet the high requirements of holographic displays. Liquid Cristal on Silicon (LCoS) devices, for example, allow phase modulation in analog mode but they fail to achieve the desired high frame rate due to longer settling times, typically in the range of hundreds of microseconds or even milliseconds [9]. They also suffer from significant non-linearity [10], strong crosstalk between neighboring pixels and phase flicker (temporal fluctuation of their phase response), which are critical aspects for holographic purposes [11]. In addition, the linear polarization required for LCoS SLMs results in a 50% reduction in photon throughput for unpolarized light sources.

On the other hand, micromirror arrays (MMAs) offer the potential for significantly better performance. However, the currently available MMAs mostly consist of tilting mirrors optimized for amplitude modulation, which is not ideal for holography. Others solutions offer too few pixels or have a pitch that is too large to meet the requirements of holography [12]. An interesting development is the fast phase modulating MMAs based on DMDs from Texas Instruments [13], but these still have quite large and few pixels for holographic applications.

In this context, the EU-funded project REALHOLO [14] is currently working on an innovative MMA for holographic displays based on comb drive MEMS actuators that can fulfil tight requirements of the optical and mechanical performance and the high level of integration. A use case application for an automotive Head-Up Display (HUD) is depicted in Figure 1. The MMA specifications, e.g. regarding pixel size, matrix array size, frame rate and mirror deflection, needed to obtain a high-quality holographic image for such an application are shown in Table 1.

Table 1: MMA specifications and chip schematics

Parameter	Value
pixel count	4000 x 2400
pixel size	4 µm x 6 µm
frame rate	> 1 kHz
deflection range	0 … 350 nm
deflection precision	8 bit
mirror tilt	< 0.1 °
mirror planarity (RMS)	<10 nm
driving voltage	0 … 3.3 V
bias voltage	3 … 4 V
power dissipation	< 2.5 W

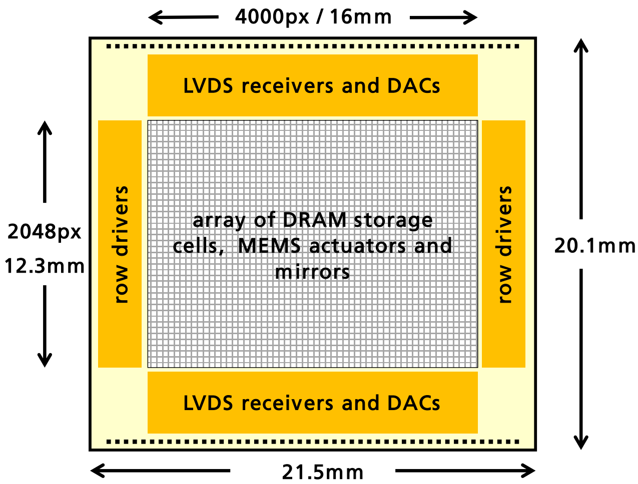

Such a complex device with a large amount of pixels requires the functionalities provided by a CMOS (complementary metal oxide semiconductor) backplane, which is capable of delivering a voltage range from to 0 V to 3.3 V to address the pixels individually. In order to enable a full 2π modulation of a RGB light sources (max. wavelength 630 nm) and to have some margin for calibration, at least 350 nm stroke of the micro mirrors is required.

2. COMB DRIVE DESIGN FOR PISTON MMA

Several design options were considered at the beginning of the project for the construction of the micromirror actuator [15]. The comb drive structure, where two sets of interdigitated fingers - one fixed and the other freely movable - act together to produce an electrostatic force, was selected as the best choice. In comparison to parallel-plate structures, large gaps in MEMS fabrication are avoided, crosstalk between neighbour pixels is minimized and the linearity of the response curves is improved. In addition, there is no risk of pull-in along the stroke direction (z-axis) [16]. The proposed MEMS comb drive design has two spring layers for an almost pure piston-mode deflection and it is depicted in Figure 2.

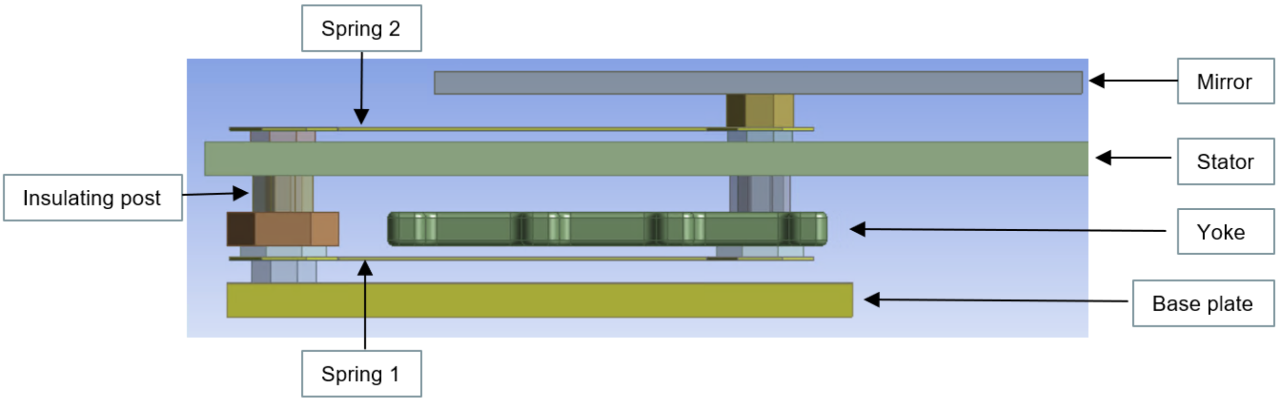

Figure 2: cross-section of comb drive micromirror actuator

The actuators with their mirrors are arranged as a tightly packed array on the backplane. Each actuator yoke is supplied with an individual voltage, while the stators of all the pixels are connected together and set to a bias voltage. The voltage difference between yoke and stator induces an electrostatic force that pulls the corresponding mirror upwards until the force balance with the mechanical force of the springs is reached. Prior to the fabrication of the final MEMS actuator on the CMOS, two types of passive devices (movable actuators without CMOS backplane) were designed for actuator and technology development and as a proof of concept. The first device, shown in Figure 3, is a small passive chip with a reduced mirror count and pin-number.

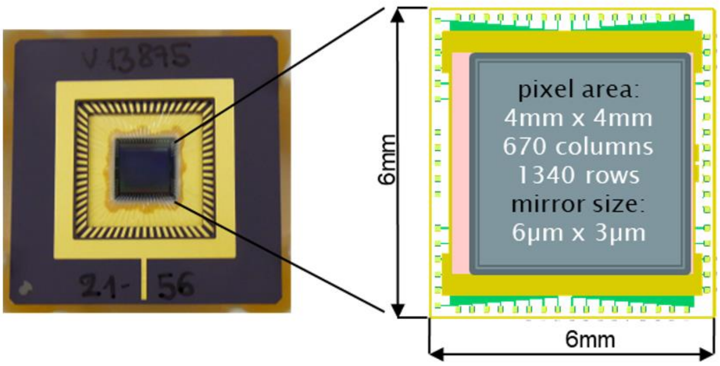

Figure 3: small passive MMA as a first proof of concept

For these small passive devices, various design options were tested, including different spring and comb geometries, spring thicknesses and gaps. The straight-spring (S-spring) type showed the best performance in the characterization tests and its fabrication process was more successful than other designs. In the second phase of the project full-size passive samples with size 2400 rows and 4000 columns were designed and developed based on the most suitable variants, see Figure 4.

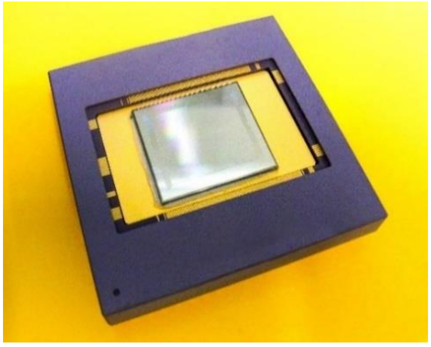

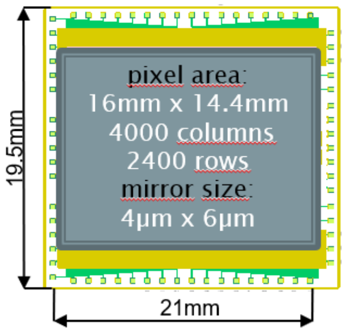

Figure 4: full-size passive MMA in a ceramic package and its general layout

The latest generation of the full-size devices were designed with a comb of 5 fingers, enabled by the recent availability of DUV lithography at Fraunhofer IPMS with its smaller minimum feature size, and a short straight spring. Figure 5 shows different generations for the S-spring type actuator: from the first design for small passives with longer springs approx. 7 µm to the newest 5-finger comb actuator with short springs (~3 µm) and a ring surrounding the pixel cell to minimize crosstalk effects with neighbour cells.

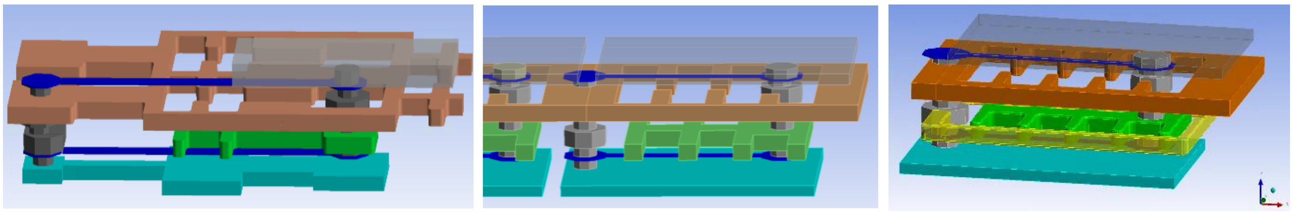

a) b) c)

Figure 5: S-spring actuator designs: a) for small passive device and b) 4-fingers and c) 5-finger actuators for full size devices

In Figure 6 the Scanning Electron Microscope (SEM) image on the left shows a portion of the fabricated pixel array without the mirror layer for better visibility of the actuator. On the right side a close-up of a 5-finger comb pixel cell is shown (corresponding to the design in Figure 5c). There are still improvements to be carried out in the technology development process to optimize the device performance and precision.

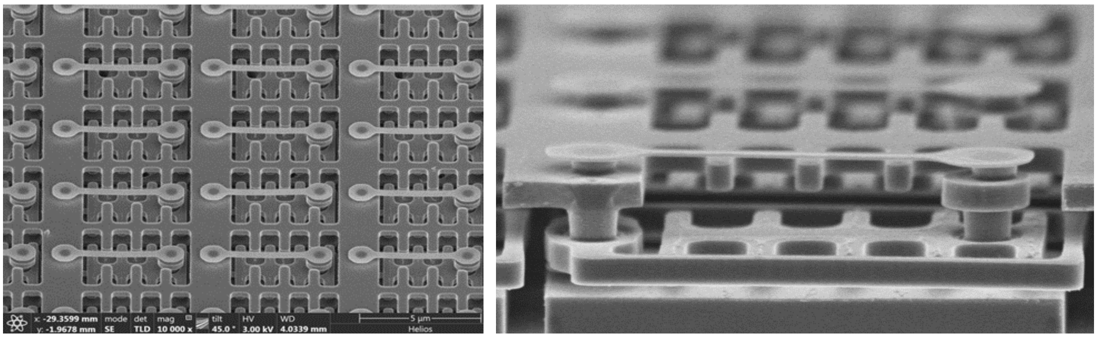

Figure 6: SEM Images of straight-spring actuator: 4-fingers comb (left) and 5-fingers comb and shield ring (right)

3. CHARACTERIZATION OF COMB DRIVE PISTON ACTUATOR

The first results with the small passive devices were presented in [17], where several tools and approaches for the MMA characterization were also discussed.

After the manufacturing, dicing and assembly processes, the characterization starts using a digital microscope (Keyence VHX-7000) for an optical inspection to confirm the cleanliness of the sample and to obtain an overview of the mirrors surface.

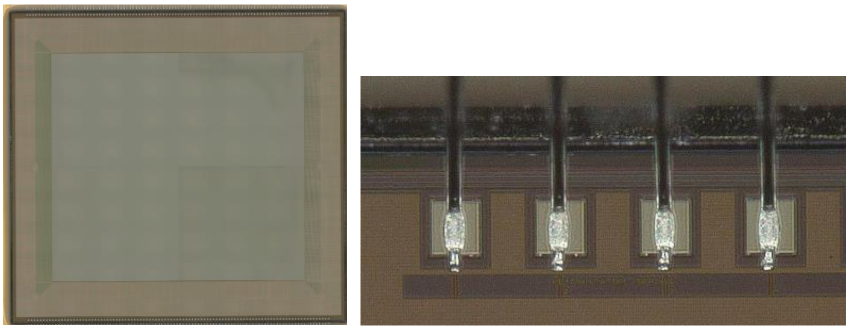

Figure 7: digital microscope images: MMA array and periphery (left), close-up of 4 bonding wires (right)

3.1 WLI-Characterization

Afterwards, a white light interferometer (Zygo NV7300) is employed for the electromechanical characterization of the MMA and the quasi-static response curves of the micromirrors were evaluated. The diagram of the laboratory set-up is depicted in Figure 8. The addressing electronics, developed specifically for the characterization of these MMAs, allow the control of the mirrors in a columnwise manner. The mirrors are addressed by the voltage V_{pix} provided by the channel 1 of the Agilent U2723A Source Measurement Unit (SMU) through the switch matrix units M1 and M2. Both switch matrices have eight output lines, each addressing the particular mirror columns. The Stator Voltage V_{stat} is provided through channel 2 of the switch matrix and set to 0 V for the following measurements. The switch matrix can be addressed using the Graphical User Interface (GUI) to generate the desired column pattern of the mirrors.

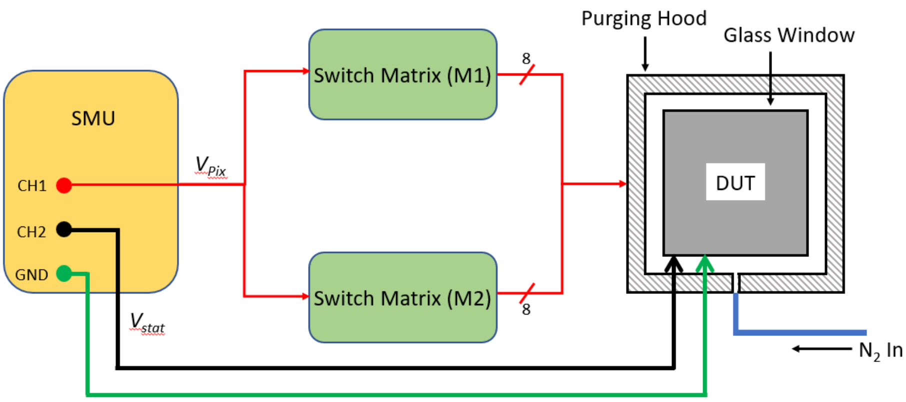

Figure 8: schematic of full-size passive measurement set-up

In Figure 9 the Device Under Test (DUT) is placed under a 50x objective lens. During measurements the MMAs are protected with a sand-blasted stainless steel frame holding a cover glass, which also makes possible the device purging with nitrogen in order to protect the DUT from the environmental moisture. In that way the stiction probability of the mirrors and any corrosion issues are minimized.

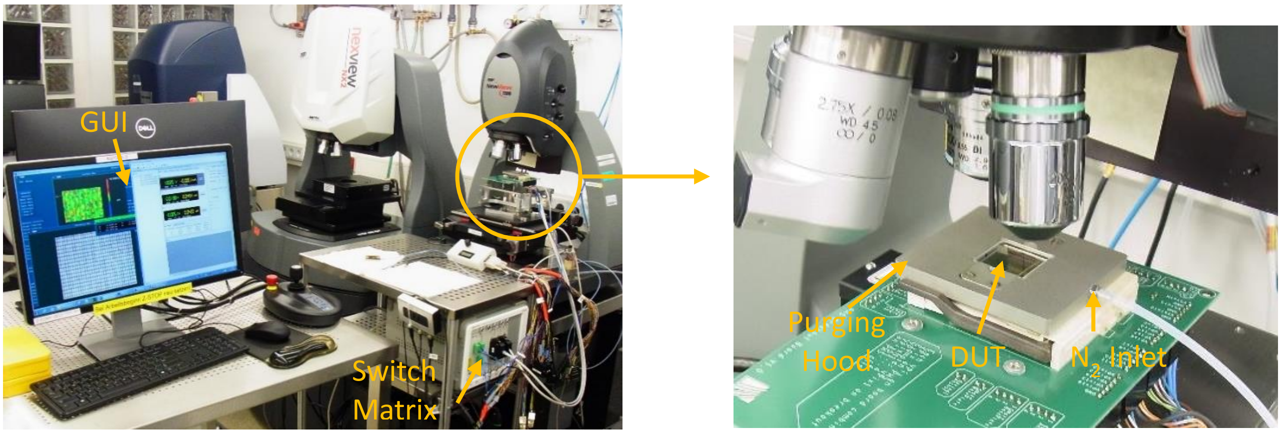

Figure 9: actual measurement laboratory setup

An example of height profile data obtained with the WLI is shown in Figure 10. A pattern recognition algorithm is used to separate the individual mirrors by masking the data of the mirror slits and then mirror parameters like z-displacement, tilt, and mirror planarity are extracted. In the left graphic a measurement field (MF) of 22 x 25 mirrors of a full-size device is depicted, when 0 V is applied to the actuators and all mirrors are in the start position. The histogram of the initial z-positions of the micromirrors in Figure 10b helps to quantify the mirror-to-mirror variation in MF due to some imperfections in fabrication process at this early developement stage.

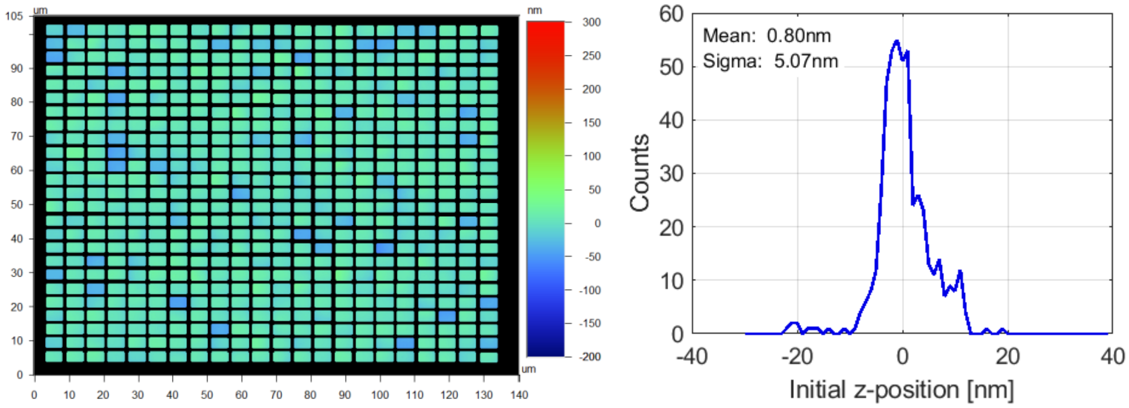

a) b)

Figure 10: WLI height profile data: a) MF with micromirros at 0 V and b) initial z-position histogram

Moreover, in order to record the response curve of the micromirrors under addressing, several measurements were carried out incrementing the voltage on the yoke. As an example, Figure 11a depicts the response curves of three single micromirrors with 4-finger actuator and 300 nm gap. The z-position values are gained in relation to several reference mirrors in MF which are keep at 0 V addressing and not moving, that makes that the response curves starts around 0 nm mirror displacement. Here the differences between the initial z-positions can be seen as well. Further work in the fabrication process is still in progress to minimize this variations and ensure a better homogeneity across the MMA. First investigations regarding deflection stability are shown in Figure 11b where the measurements during the ramp-down match very well with the ramp-up response curve.

In terms of the mirror planarity very good results have been already achieved at the current project stage. Typical RMS values for the surface height profile < 2nm (deviation with respect to a plane fit into each mirror) for a MF of 512 mirrors are shown in the histogram of Figure 12. That already fulfills the mirror planarity requeriment in Table 1.

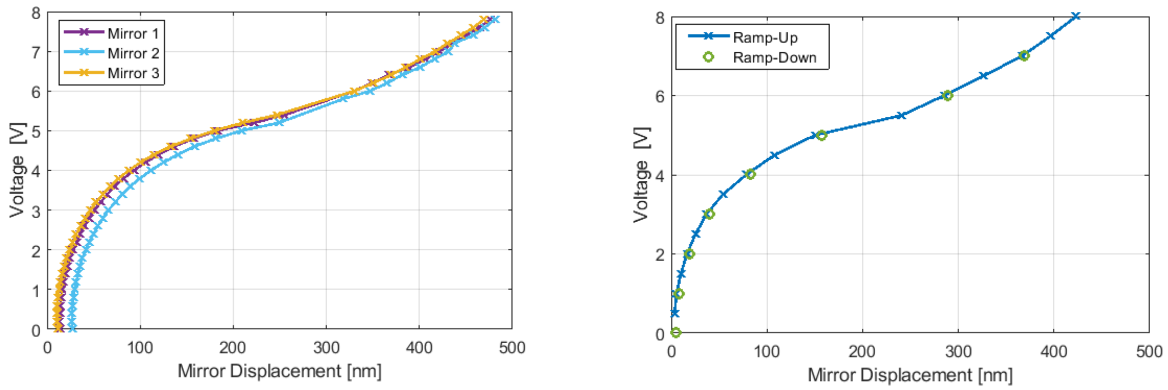

a) b)

Figure 11: a) measured response curves of three 4-finger actuators, b) Ramp-Up and Ramp-Down response curves

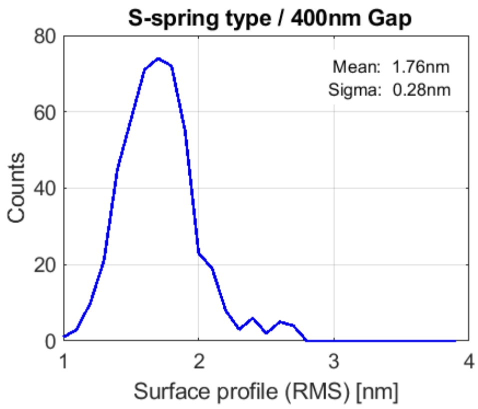

Figure 12: MMA Surface profile (RMS) for 5-finger design with a 400nm gap

3.2 LDV-Characterization

In order to evaluate the dynamic behaviour of the micromirrors, the resonance frequency and damping for single actuators were analyzed by means of laser-doppler vibrometry measurements (Polytec MSA-500). The mirrors where addressed with a square wave signal of 6 V with a frequency of 10 kHz and a duty cycle of 30%.

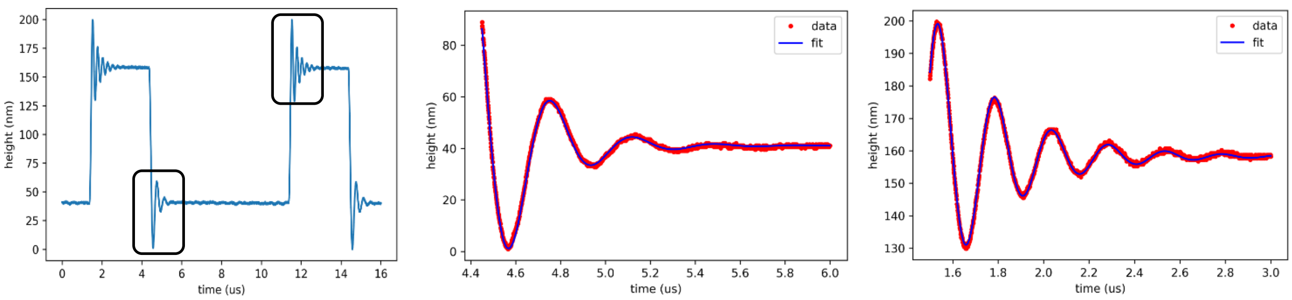

a) b) c)

Figure 13: a) dynamic mirror behaviour, b) close-up for downward movement and c) close-up for upward movement

Figure 13a depicts the mirror movement measured when a 6 V square signal is applied to the yoke for two addressing cycles. The mirror oscillation after the downward mirror movement in Figure 13b shows the mirror behaviour when the yoke voltage is at 0 V. This can be used to calculate the natural frequency of the actuator itself, as withouth electrical fields only the mechanical force of the springs is present. A resonance frequency value f_{res} ~ 270 kHz and a damping factor ζ of ~ 0.2 has been found, calculated by fitting the measurement data with a damped harmonic oscillator model according to

$$\alpha(t) = c_1 e^{-c_2 t} \cdot \cos(c_3 t + c_4) + c_5$$
$$\text{with } f_{res} = \frac{c_3}{2\pi} \text{ and } \zeta = \frac{c_2}{c_3}.$$

The frequency for the upward mirror movement is higher than the natural resonance frequency, as the electrostatic field at the high voltage of the square signal contributes an additional restoring force in this case (see Figure 13c). In contrast to a parallel plate actuator, where the electrostatic force increases with the deflection and therefore decreases the effective natural frequency at larger deflections, the comb drive principle has a decreasing electrostatic force at high deflections and therefore increases the natural frequency in the upper state. This effect will depend on the desired end position of the mirror itself.

Figure 14 shows a simple approach to reduce the overshoot of the actuator by increasing the rise time of the addressing voltage from 5 ns (Figure 14a) to 3 µs (3000 ns, Figure 14b). It shows that the overshoot could be reduced. For an even more effective reduction of the settling time an advanced addressing scheme like input shaping can be used.

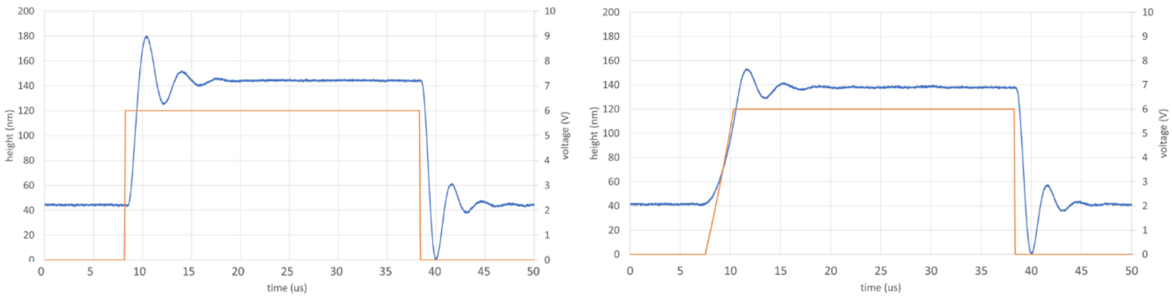

a) b)

Figure 14: dynamic behavior of the actuator (blue) with the corresponding driving voltage (orange) with a rise time of: a) 5ns and b) 3µs

4. FEM SIMULATIONS AND COMPARISON WITH MEASUREMENTS

The response of the actuator depends on several geometrical parameters such as the finger widths of the comb structures, thickness and width of the spring, initial distance between stator and yoke etc. In this section, the response of the actuator is investigated through parametric variations. Both the electrostatic force F_{el} between the stator and the yoke parts and the mechanical force F_{mec} of the spring together define the response curve. However, it takes a high effort to assess both these forces from different physical domains within the same finite element method (FEM) simulation run. Therefore, simulations were performed for these two forces independently and we get the response curves later from the force equilibrium. The results presentet here are valid for the full size passive device with 4-fingers comb structure, Figure 5b. All simulations presented in this section are performed with ANSYS Workbench 2023/R1. We also compare the simulation to the measured response of fabricated samples and derive the deviation of the geometrical parameters from their design values. It also allows us to select the best operating region in terms of linearity and operating voltage range.

The electrostatic force F_{el} in the actuator is simulated in a surrounding air box whose dimension is equal to the pixel size. This box has mirror boundary conditions, so the effect of the neighboring pixel geometry is implicitly considered here for the same addressing state (for cross-talk simulations see [16]). The simulations are all performed for a specific potential difference U_{ref} between the yoke and the stator for a number of yoke positions. The resulting curve can then be scaled to any other addressing voltage as the electrostatic force is proportional to the voltage squared for a given geometry.

The mechanical force F_{mec} is found from static structural simulations by applying various loads to the FEM model. We find a very good linearity for the full range of design parameters and deflections, meaning that we operate within Hook's law. Therefore the stiffness can be calculated as a spring constant.

Figure 15a shows an example of F_{el} curves for different potential difference at various yoke positions, as well as a straight line for F_{mec} (corresponding to a spring stiffness of 50 nN/µm). Each point where the F_{mec} line intersects an F_{el} curve represents the force equilibrium for the respective voltage and position. E.g., F_{mec} coincides with F_{el} curve for 6.6 V at 120 nm. The pixel response curve, as shown in Figure 15b, is generated from these intersection points of the two force curves and would be valid for the designed geometry of the device.

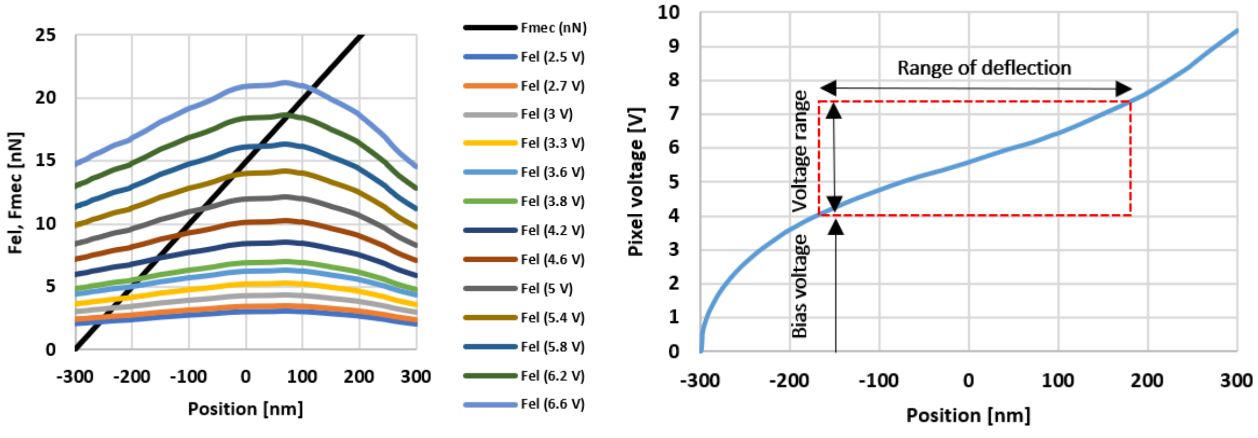

a) b)

Figure 15: a) simulated data for F_{el} and F_{mec} and b) calculated response curve (voltage vs position) using the force equilibrium points

When there is no potential difference between the stator and the yoke, there is no electrostatic force and the yoke stays at the initial position, in this example -300 nm position. As a zero point for the position axis we chose the situation where the upper face of the yoke and the lower face of the stator lie in the same plane. In this example geometry the stator and the yoke have a thickness of 300 nm each and thus are fully overlapped at position 300 nm. One would expect the electrostatic force to be zero at this position due to symmetry, but obviously the asymmetric surrounding of the combs – the base plate below at yoke potential and the mirror above at stator potential – still has a very strong impact so that the simulated F_{el} is reaching zero only at a much larger deflection.

The red box in Figure 15b indicates an operating region of 350 nm of stroke. The lower edge of the box is given by the bias voltage that is common for all pixels of a device and constant in time. The height of the box represents the required operating voltage range which is individual for each pixel. This operating voltage range is limited by the voltage that the backplane CMOS circuitry which will be used in an active device in future can provide (3.3 V).

4.1 Selection of suitable region for operation

Although the ideal response of an actuator is linear, certain non-linearities are unavoidable in case of electrostatic actuators. For a full 2π phase modulation of visible light we need an actuator stroke of 350 nm. By varying the bias voltage, we can optimize the operating region for best linearity. The boxes in Figure 16a represent some examples. We quantify linearity within our operating region by calculating the 'loss of resolution'. It is explained in more detail in [16].

$$\text{Loss of resolution} = log_2\left(\frac{average\ slope}{minimum\ slope}\right)\ [bit]$$

Here the average slope is the slope of a straight diagonal of a considered box of operation, e.g. inside the red box in Figure 16a. The smallest slope within that region (slope triangle) represents the worst case actuator position: here any inaccuracy ΔU in the addressing voltage causes the greatest error Δz in the actuator position.

The ratio between these two slopes gives the factor of how much more precise the addressing voltage has to be compared to the desired accuracy in position. Taking the $\log_2$ of this tells us how much more bits the voltage resolution should have compared to the desired resolution in position. Figure 16b shows the calculated loss of resolution for different operating regions of 350 nm stroke vs. the corresponding start position of the stroke (which in turn would be defined by the chosen bias voltage). For example, the first point in the curve (Figure 16b) is the loss of resolution withing the operating region starting at -250 nm (red box of operation in Figure 16a. Figure 16b also gives the best linearity at a start position of around -170 nm for this set of design parameters. The loss of resolution is well below 1 bit, which is really excellent for an electrostatic actuator.

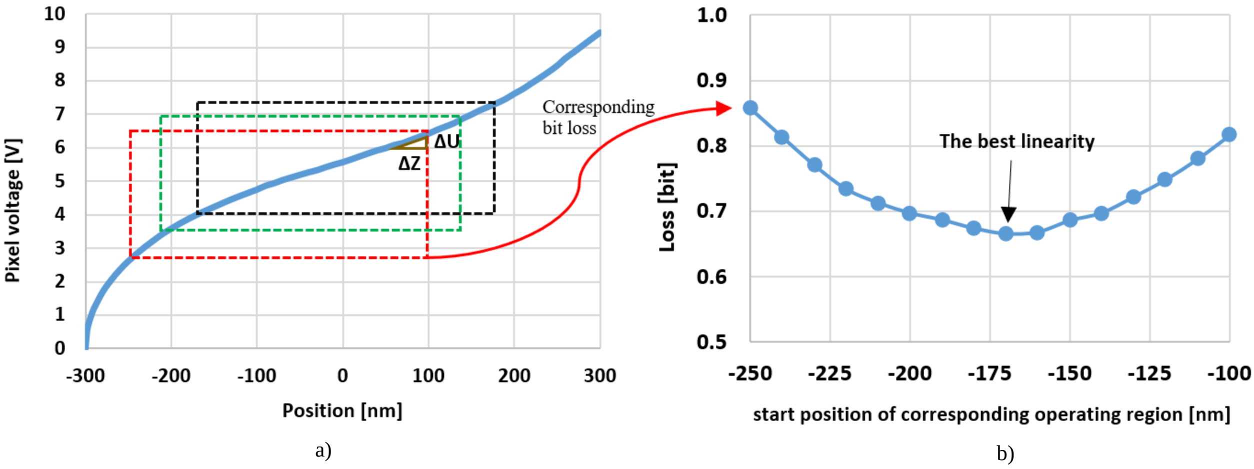

Figure 16: loss of precision for different operating region of 350 nm stroke vs. the corresponding start position

The operating voltage range is another important parameter to select the best region, the lower is the better. For a constant stroke length, the average slope of an operating region is proportional to its voltage range. As the minimum slope always lies withing the reasonable boxes of operation, the least voltage range is also achieved for the same start position where the best linearity occurs.

4.2 Effect of parametric deviations in pixel response

Spring width and thickness

From beam-bending theory it is known that the stiffness should increase linearly with the width and proportional to the cube of the thickness of the spring. For visualization, we present here a comparison of response curves, only for two variations in width/thickness. Figure 17a shows the effect on voltage range for a specific stroke length due to a width variation and Figure 17b shows the change in displacement at a specific voltage range due to the variation in thickness. Several simulations were performed in a similar manner to understand the effect of geometrical variation in pixel response. These two curves are represented here only as examples. The general effect of a changed spring stiffness is that the response curves are essentially stretched along the y axis (red arrow).

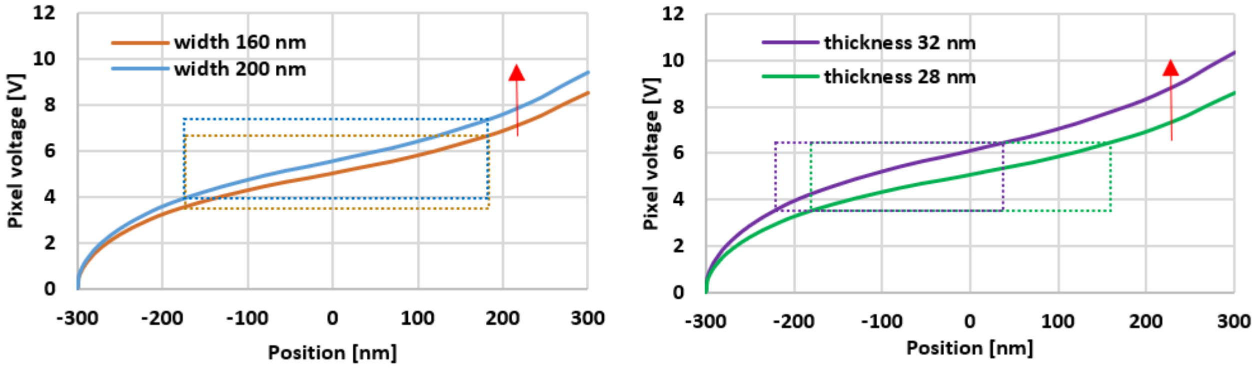

a) b)

Figure 17: exemplary deflection curves a) for 160 nm and 200 nm spring width and b) for 32 nm and 28 nm spring thickness

Horizontal gap (HG)

The horizontal gap is defined as the lateral distance between the neighbor fingers of the stator and the yoke as seen from above. Figure 18 shows the actuator responses simulated for two horizontal gap values. As smaller gaps yield larger electrostatic force, the required operating voltage range is smaller in this case. It is perceptible from the figure that the effect is small at the starting and the ending of the curve, while being larger in the middle section. A reduction in HG basically bends the curve in the direction of red arrow rather than shifting it in x or y direction.

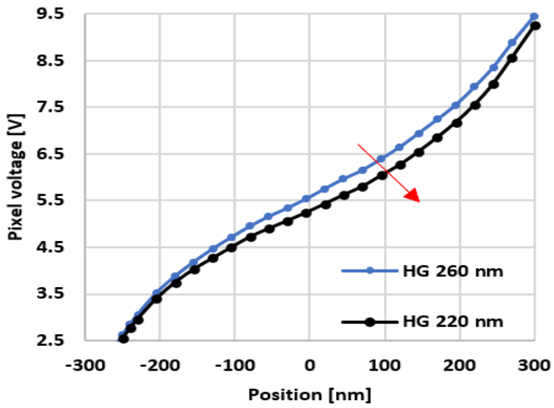

Figure 18: deflection curves for two different horizontal gaps (HG) between yoke and stator fingers

Initial distance

The initial distance is the vertical distance between the stator and the yoke when no voltage is applied. Ideally this is equal to the thickness of the sacrificial layer between the yoke and the stator. However, the two springs may bend up or downwards after fabrication due to internal stress gradients which leads to a change of the initial distance.

We can select a start position of a range of operation by choosing an appropriate bias voltage. For a larger initial distance a higher bias voltage is needed to reach the same start position of the stroke. However, due to the electrostatic forces being proportional to the total voltage squared, a lower operating voltage range is needed to cover the desired stroke in that case. Figure 19b demonstrates a comparison between bias voltages and operating voltage ranges for the device with two initial distances as an example. Each start position in the figure corresponds to an operating region of 350 nm stroke, which means that different end positions will be reached. The needed addressing voltage range is considerably lower, regardless of the operating region, in case of a 400 nm compared to 300 nm initial distance.

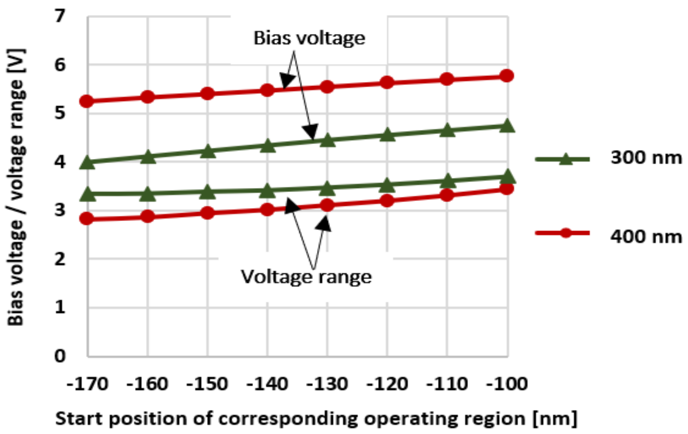

Figure 19: needed bias voltage to reach a start position of the operating range as well as the then needed voltage range to reach the 350 nm stroke for an initial distance of 300 nm or 400 nm

4.3 Modal analysis

Modal analysis is not only important for the design optimization but also to understand the dynamics of the device. Natural frequencies provide a conception how the device will react to certain excitations. The application of the addressing voltages will happen in a step-wise shape with a certain rise and fall time. The frequency spectra of such an excitation covers a wide range going from low frequencies up to a certain threshold, determined by the steepness of the voltage pulse. Therefore, it is best that the target mode has the lowest frequency of the spectrum and therefore will be excited best by the voltage pulse and that the frequencies of the unwanted modes of vibration are much higher.

Modal analysis of the FEM model is performed to extract the natural frequencies and modes of vibration. Figure 20a-e represents the 5 lowest frequency modes of one example geometry. As has been desired, the first mode, the one with the lowest overall frequency, is the piston mode with 212 kHz. This mode is the one that will be used during operation of the chip.

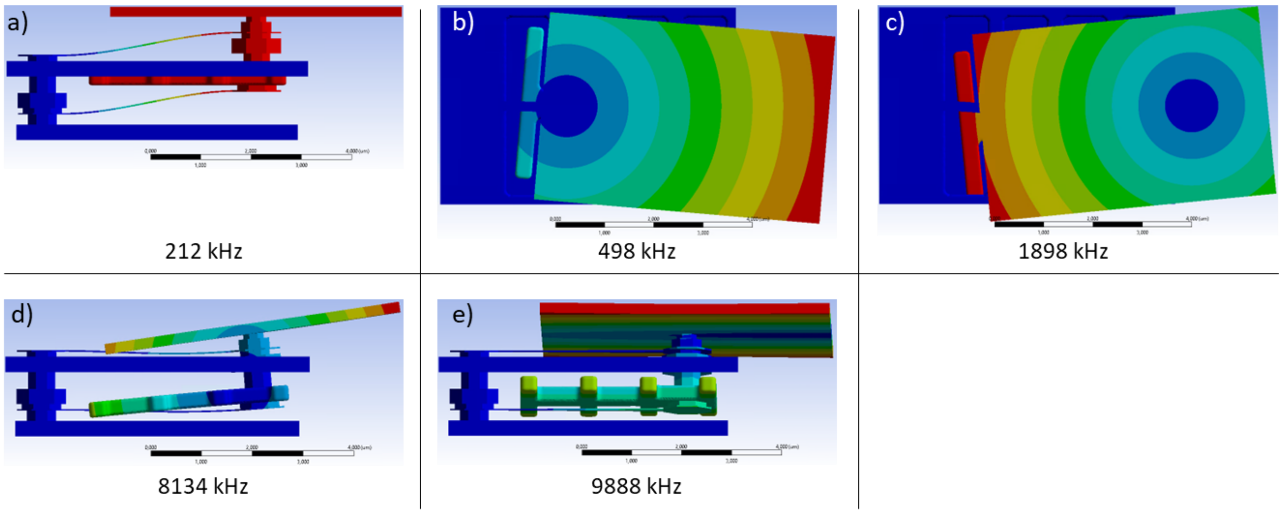

Figure 20: a) piston mode b) and c) are two rotational modes about different z-axes and d) and e) are two tilting modes about the y and x axes

The two next modes are rotations around vertical axes and are only excited if there is a lateral force component between yoke and stator. This can occur if the yoke is not placed symmetrical within the stator frame which can occur due to lithography overlay errors or due to statistical feature edge roughness. Rotations around vertical axes have very little optical influence in the application as the phase of the reflected light is not changed. The next two modes with even higher frequency both are tilting modes that do have unwanted optical effects. However, at frequencies much higher than the piston mode, 8134 kHz and 9888 kHz, respectively, the actuator is already quite robust against any disturbance that may cause tilting and only small effects would be expected in regular operation of the MMA. With these numbers it can be concluded that a safe operation is quite feasible without exciting unwanted/parasitic modes.

4.4 Fit of simulation to the measurement

In this section, the simulated response curves of the passive device are fitted to the measurement curves. A fitting routine is developed to determine the change in critical geometry parameters. The fitting parameters, horizontal gap h, spring stiffness k, initial distance d and position shift s of the measurement are varied by iteration for the fitting. The simulated response curve is generated according to the equation below and fitted to the measured response curve with position shift ($z =$ relative measurement position $- s$).

$$U\,(z) = U_{ref} \times \sqrt{\frac{(z-d)\ \times k}{F_{el,ref}(z,h)}}$$

Here U_{ref} is the reference potential difference at which the electrostatic force is simulated and $F_{el,ref}(z,h)$ is the simulated electrostatic force for a horizontal gap h at position z for the reference voltage.

Figure 21a shows such an example measured response curve with z-position values (relative to references mirrors). To fit to the simulated curves with their absolute z-position values, an adequate position shift of all data points will be needed. That corresponds to the fit parameter position shift s. In simulations the position of the yoke at 0 V is varied. In Figure 21b an example starting at -300 nm is shown, which is the typical design value of the thickness of sacrificial layer between stator and yoke. Within real samples this distance may be different due to an inaccuracy of the sacrificial layer deposition and/or due to stress gradients bending the hinges. This parameter of fitting along x axis is the initial distance d, different from the position shift s. As the electrostatic force vanishes for some high position z_p of the actuator, a force equilibrium can then not be reached any more even with very large voltages. The simulated response curves will therefore have a pole at that absolute position z_p. The effect of a varying initial distance essentially is to stretch the response curve along the x-axis from the fixed position of the pole. A modification in spring geometry is considered in the fit parameter stiffness k and changes the slope of the F_{mec} line. This results approximately in a stretching of the response curve in y direction (Figure 17). The fit parameter horizontal gap h takes into account finger width deviations, differing slightly from the design value, due to lithography imperfections. (Figure 18).

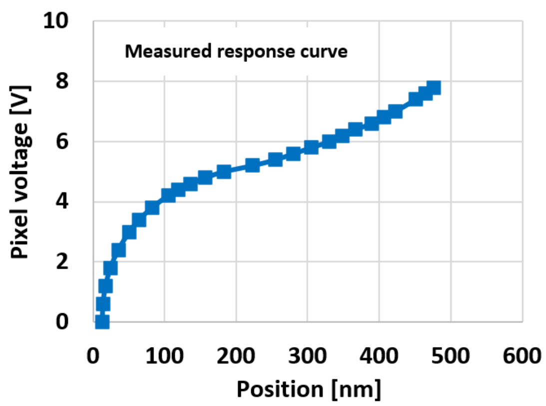

a)

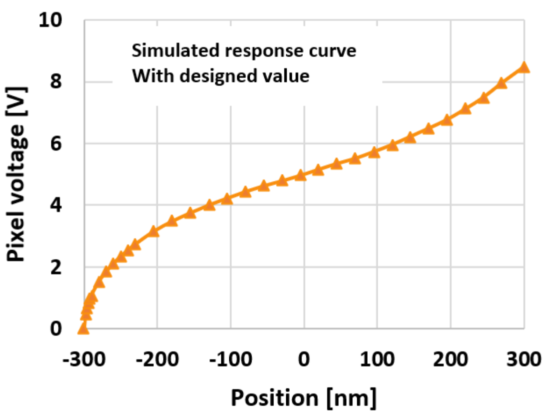

b)

Figure 21: a) measured deflection curve and b) simulated response curve with default design

Using these four parameters we can already get a quite good fit of our measured curves. This enables the extraction of the parameter values for the specific sample under test. Obviously, there are more geometry parameters that might deviate from the design values and that also have an influence on the response curve, like for example the thicknesses of the yoke and stator but at this stage they are less relevant.

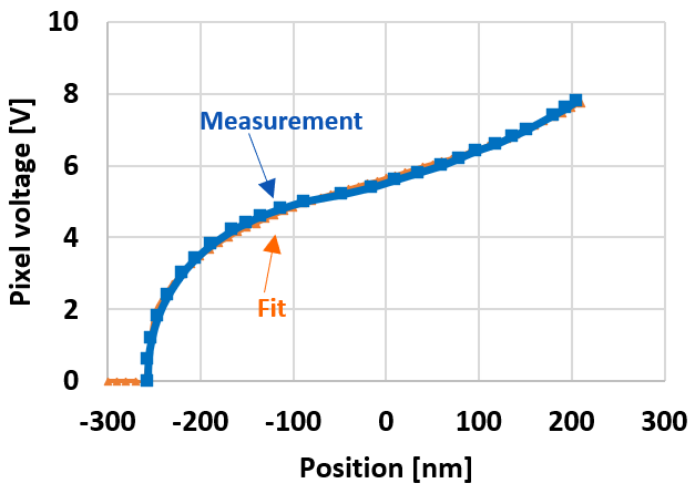

Figure 22: measured response curve and best fit simulated curve

Figure 22 shows the measurement curve and the fit for a specific pixel. The best fit was found at -255 nm initial distance indicating that the springs are deformed/bend slightly upwards. The measurement position shift is -270 nm. The fit also yielded a value for the spring stiffness of 46 nN/µm, close to the design value of 49.7 nN/µm and 220 nm for the horizontal gap, where 240 nm was the design value.

5. CONCLUSIONS

In this paper we report the latest characterization results of a novel micro mirror array (MMA) spatial light modulator (SLM) device, based on an electrostatic comb drive actuator design featuring two sets of interdigitated fingers. This MMA type has the potential to fill the current technological gap to achieve real holographic displays.

The properties of MMA pixels were measured using white light interferometry and laser vibrometry. Response curves of recently fabricated samples are presented: a micro mirror displacement of 350 nm in piston mode is well achieved making possible a full 2π phase modulation of an RGB source. For this an addressing voltage of 3.3 V, which is available from a future CMOS backplane circuit, is sufficient, together with an additional global bias voltage of 3-4 V applied to the stator. First response curves of the proof-of-concept devices showed a good agreement with the FEM simulations. The actuator features a close-to-linear response within the designated range of operation. This is quite uncommon for an electrostatic actuator, but a strong benefit of the actuator concept presented here. In addition further simulations were done varying actuator parameters such as spring width, spring thickness and horizontal gap between comb fingers to understand the dependencies and prepare for adaptation of future MMA generations to other applications. Regarding the dynamic behaviour, resonance frequencies around 270 kHz and damping factors of 0.2 were measured for the desired piston deflection mode. This also matchs the FEM simulations very well and allows high frame rates compatible with time-sequential generation of RGB images.

Currently we are continuing the MMA development by improving the precision and reliability of our manufacturing processes. Characterization will continue with more samples of newer wafer lots to get information on more details as well as parameter variations and statistics. Nevertheless, the results presented here already show the principal suitability and potential of our novel MMA devices for real holographic 3D displays.

ACKNOWLEDGEMENTS

The project REALHOLO has received funding from the European Union’s Horizon 2020 research and innovation program under grant agreement No. 101014977. It is an initiative of the Photonics Public Private Partnership. Thanks to the REALHOLO project team for the fruitful discussions supporting the current work and to the IPMS SLM development and fabrication teams for providing the test devices.

REFERENCES

[1] GABOR, D., “A new microscopic principle,“ Nature 161(4098), 777 (1948).
[2] Blinder, D., et al., “Signal processing challenges for digital holographic video display systems,“ Signal Processing: Image Communication 70, 114–130 (2019).
[3] Slinger, C., et al., “Computer-generated holography as a generic display technology,“ Computer 38(8), 46–53 (2005).
[4] Rückerl, F., et al., “Spatio-angular light control in microscopes using micro mirror arrays,“, Proc. SPIE 93052Y (2015).
[5] Burge, J. H., “Applications of computer-generated holograms for interferometric measurement of large aspheric optics,“, Proc. SPIE 2576 (1995).
[6] Häussler, R., et al., “Large real-time holographic displays: from prototypes to a consumer product,“, Proc. SPIE 72370S (2009).
[7] Reichelt, S., et al., [Holographic 3-D Displays - Electro-holography within the Grasp of Commercialization], InTech (2010).
[8] Zschau, E., et al., “Generation, encoding, and presentation of content on holographic displays in real time,“, Proc. SPIE 76900E (2010).
[9] Wu, W., et al., “LCOS Spatial Light Modulator for Digital Holography,“ Photon.Lett.PL 13(4), 76 (2021).
[10] Tong, Y., et al., “Improvements of phase linearity and phase flicker of phase-only LCoS devices for holographic applications,“ Applied optics 58(34), G248-G255 (2019).
[11] Yang, H. and Chu, D. P., “Phase flicker in liquid crystal on silicon devices,“ J. Phys. Photonics 2(3), 32001 (2020).
[12] “Deformable Mirrors,“, https://bostonmicromachines.com/products/deformable-mirrors/standard-deformable-mirrors/ (15 December 2023).
[13] Bartlett, T. A., et al., “Adapting Texas Instruments DLP technology to demonstrate a phase spatial light modulator,“, Proc. SPIE 109320S (2019).
[14] “REALHOLO project,“, https://realholo.eu/ (9th January 2024).
[15] Li, L. and Chew, Z. J., [Microactuators: design and technology], Elsevier, 305–348 (2014).
[16] Dürr, P., et al., “MEMS piston mirror arrays for computer generated holography,“, Proc. SPIE 1201306 (2022).
[17] Nitzsche, M., et al., “First Characterization of Comb Drive Based Micro Mirror Arrays,“, Proc. MikroSystemTechnik Kongress (2023).